International Journal of Heat and Technology
Vol. 44, No. 2, April, 2026, pp. 703-716
Journal homepage: http://iieta.org/journals/ijht

Thermodynamic Evolution and Operational State Detection in Solid Oxide Fuel Cell Systems: Modeling and Analysis

Cuili Mao*, Shanshan Yi, Jingfan Wang

School of Intelligent Manufacturing, Nanyang Institute of Technology, Nanyang 473004, China

Corresponding Author Email: maocuili@nyist.edu.cn

https://doi.org/10.18280/ijht.440223

Received: 9 November 2025
Revised: 17 March 2026
Accepted: 26 March 2026
Available online: 30 April 2026

Keywords:
solid oxide fuel cells, thermodynamic behavior evolution, entropy production rate, condition monitoring, nonlinear observer, physics-informed neural network

ABSTRACT

Solid oxide fuel cells (SOFCs) are recognized as highly efficient and clean energy conversion devices. However, during long-term operation, irreversible thermodynamic behaviors—such as electrochemical reactions, heat transfer, and mass transport—lead to continuous system performance degradation, posing a major barrier to commercialization. Conventional operational state detection methods predominantly rely on macroscopic electrical parameters, which lack the sensitivity required for early-stage fault warning. Moreover, existing thermodynamic modeling and condition monitoring frameworks often remain decoupled, failing to establish a direct linkage between irreversible evolution mechanisms and system health status. To address these limitations, this study adopts entropy production rate as a unified physical metric and integrates nonequilibrium thermodynamics, multi-scale dynamic modeling, and nonlinear state estimation theory to develop an operational state detection model that ensures both physical consistency and online feasibility. A hybrid-dimensional thermodynamic dynamic modeling approach is proposed to effectively balance model fidelity and computational efficiency. Explicit correlations between entropy production components and measurable variables are established, enabling the extraction of entropy fingerprints to accurately characterize different degradation modes. A novel entropy observer is designed by fusing the Square-Root Unscented Kalman Filter (SR-UKF) with electrochemical impedance spectroscopy, allowing precise online estimation of system irreversibility. Furthermore, a physics-informed neural network hybrid model embedded with physical constraints is constructed, significantly improving modeling accuracy under complex degradation scenarios. This research advances the role of entropy production rate from a traditional efficiency indicator to a core metric for online condition monitoring, extends the engineering application of nonequilibrium thermodynamics in complex energy systems, and provides theoretical support and technical methodologies for the efficient and stable operation of SOFC systems.

1. INTRODUCTION

Solid oxide fuel cells (SOFCs) [1, 2], as highly efficient and clean energy conversion devices, can directly convert the chemical energy of fuels into electrical energy. They possess significant advantages such as high energy conversion efficiency, zero carbon emissions, and wide fuel adaptability, demonstrating broad application prospects in distributed energy, transportation, aerospace, and other fields. As such, they have become one of the important technological pathways for addressing energy crises and environmental issues [3, 4]. However, during long-term operation, SOFC systems inevitably experience irreversible thermodynamic behaviors coupled with multiple processes, including electrochemical reactions [5, 6], heat and mass transfer [7], and charge transport [8]. The accumulation of these irreversible processes leads to a series of performance degradation phenomena, such as electrode aging, electrolyte deterioration, and decreased interface reaction activity [9-11], which directly shorten system service life and reduce operational reliability, becoming the core bottleneck restricting their commercial promotion. From a thermodynamic perspective, the essence of system performance degradation lies in the continuous intensification of irreversible processes. The entropy production rate [12, 13], as a core thermodynamic indicator characterizing irreversibility, can quantify the intensity and evolution laws of various irreversible processes. Establishing a real-time mapping relationship between entropy production rate and system operating status enables closed-loop control of evolution mechanisms, state detection, and early warning. This not only represents a key breakthrough in solving the practical application challenges of SOFCs but also serves as an important extension of nonequilibrium thermodynamics theory in the field of complex energy equipment engineering. The core value of this study lies in breaking through the limitation of traditional entropy production rates being used merely as efficiency evaluation tools, upgrading it to a core

indicator for online state monitoring. Through the deep integration of thermodynamic mechanisms and engineering detection technologies, this work enriches the application scenarios of nonequilibrium thermodynamics in energy systems, providing solid thermodynamic theoretical support and engineering technical methods for the efficient and stable operation of SOFC systems.

Although domestic and international scholars have conducted extensive research on the thermodynamic modeling and state detection of SOFCs, existing studies still face many urgent problems, making it difficult to meet the high-precision and online requirements of practical engineering applications. First, the thermodynamic modeling and state detection links are disconnected from each other. Traditional research mostly treats them separately. Steady-state thermodynamic models [14] have simple structures but fail to capture the evolution laws of thermodynamic characteristics during dynamic system operation [15]; meanwhile, dynamic modeling has not been deeply integrated with state detection. At the same time, existing state detection methods mostly rely on macroscopic electrical parameters such as voltage and current [16, 17], ignoring the entropy production rate as the core measure of irreversibility. This results in a clear disconnect between measurable variables and system health status, making it impossible to achieve accurate identification of early degradation. Second, the contradiction between modeling accuracy and computational efficiency is prominent. Three-dimensional computational fluid dynamics (CFD) models [18] can accurately capture temperature and concentration gradients as well as entropy production distribution inside the stack, offering high fidelity, but the calculation process is cumbersome, with solution times typically reaching the minute level, making it difficult to meet the real-time requirements of online monitoring. In contrast, traditional lumped parameter models are computationally efficient but ignore temperature gradients along the flow direction of the stack, failing to accurately characterize thermal stress distribution and local entropy production characteristics. This leads to significant deviations between model predictions and actual thermodynamic characteristics, making it difficult to support high-precision state detection [19]. Third, state observation methods exhibit obvious limitations. Traditional linear observers [20] struggle to adapt to the strong nonlinear characteristics of SOFC systems. Their inherent linearization approximations introduce large errors and are prone to estimation divergence, preventing stable estimation of entropy production rates. Meanwhile, there is a lack of effective multi-source data fusion strategies, making it difficult to integrate electrochemical impedance spectroscopy and other test data reflecting internal characteristics with conventional monitoring data, thereby hindering the precise separation of entropy production components and the identification of early degradation patterns. Finally, degradation modeling lacks sufficient physical consistency. Pure data-driven models [21] can fit degradation laws using large amounts of data but suffer from poor interpretability, failing to meet the core requirements of thermodynamics journals regarding physical mechanisms. Additionally, their generalization ability is insufficient in scenarios with scarce labeled data. Pure mechanism-based models, while possessing strong physical interpretability, struggle to accurately capture the nonlinear dynamic characteristics of complex degradation processes such as nickel coarsening and chromium poisoning, resulting in modeling accuracy that fails to meet practical demands.

In response to the aforementioned research gaps, this paper conducts in-depth research focusing on the thermodynamic characteristic evolution and operational state detection of SOFC systems. The core contributions are as follows: A hybrid-dimensional thermodynamic dynamic modeling method is proposed, adopting an architecture that combines one-dimensional discretization of the stack, zero-dimensional lumping of auxiliary systems, and thermal network coupling. This approach significantly improves computational efficiency while retaining the capability to capture temperature gradients and clarifies the physical basis for the number of discretization nodes. An entropy production component decomposition and evolution characterization system is established, deriving analytical expressions for each entropy production component, proposing the concept of entropy fingerprints to accurately characterize different degradation modes, and establishing explicit correlations between entropy production components and measurable variables. A nonlinear entropy production observer based on physical information constraints is designed, employing the Square-Root Unscented Kalman Filter (SR-UKF) algorithm to solve the estimation divergence problem in strongly nonlinear systems, and combining a dual time-scale data fusion strategy to achieve online accurate estimation of entropy production rates. A physics-informed neural network-assisted hybrid degradation model is constructed, embedding thermodynamic laws as hard constraints into network training to balance physical consistency and modeling accuracy.

The logical arrangement of the subsequent chapters of this paper is as follows: Section 2 elaborates in detail on the core methodologies of the research, including hybrid-dimensional thermodynamic dynamic modeling, entropy production component decomposition and evolution characterization, nonlinear entropy production observer design, and physics-informed neural network hybrid degradation model construction. Section 3 verifies the effectiveness and superiority of the proposed models through multiple sets of comparative experiments. Section 4 analyzes the experimental results, thoroughly discussing the advantages of each innovative method and the limitations of the study. Section 5 summarizes the full text's research findings and proposes future research directions.

2. METHODOLOGY

2.1 Hybrid-Dimensional thermodynamic dynamic modeling

To achieve accurate characterization of thermodynamic characteristic evolution and online state detection for SOFC systems, it is necessary to construct a dynamic model that balances modeling accuracy and computational efficiency, addressing the core challenge that traditional modeling methods are difficult to apply online. The proposed hybrid-dimensional thermodynamic dynamic model adopts a differentiated modeling strategy, designing the architecture according to the differences in thermodynamic characteristics between the stack and the auxiliary system: the stack is discretized in one dimension along the fuel and oxidant flow directions, divided into 8–12 independent control volumes to accurately capture the temperature gradient along the flow direction; the auxiliary system adopts zero-dimensional lumped modeling, and achieves heat exchange coupling with

the stack through a thermal network. The design basis of this architecture originates from system thermodynamic characteristic analysis: the temperature gradient along the flow direction inside the stack directly dominates the distribution and evolution of irreversible entropy production, thereby affecting the system degradation process, while the internal temperature gradient of the auxiliary system is relatively small, so adopting zero-dimensional lumped modeling can simplify the model structure while ensuring computational accuracy. The number of discrete control volumes is determined based on thermal impedance theory; 8–12 nodes can fully capture the temperature gradient while avoiding computational redundancy caused by excessive discretization, laying the foundation for the online application of the model. Figure 1 shows the overall architecture of the hybrid-dimensional thermodynamic dynamic modeling for SOFC.

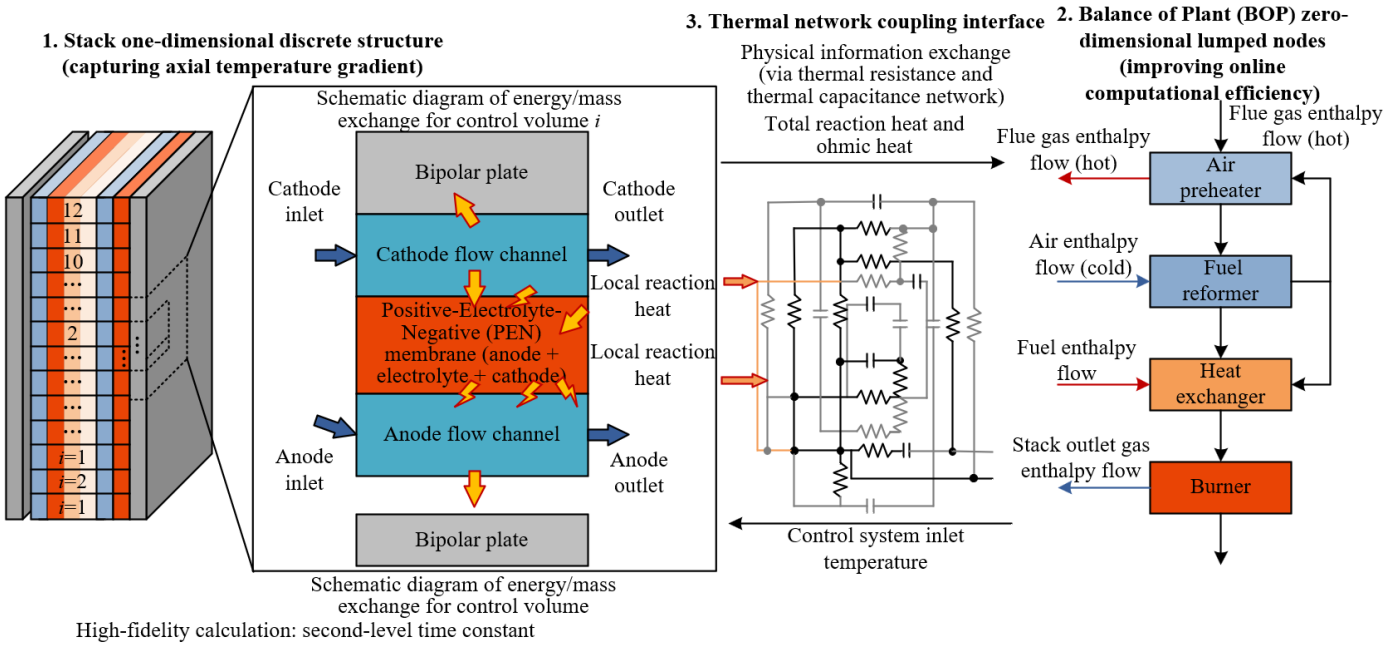

Figure 1. Architecture of the hybrid-dimensional thermodynamic dynamic modeling for solid oxide fuel cells (SOFCs)

The energy transfer and conversion process of the stack is the core of thermodynamic characteristic evolution. Based on the law of conservation of energy for control volumes, gas-phase and solid-phase energy equations are established respectively to accurately describe the thermodynamic behavior of the stack. Taking the cathode as an example, the gas-phase energy equation considers the dynamic characteristics of the one-dimensional discrete control volume, expressed as:

$$\rho_{c,i}c_{p,c}A_c\frac{\partial T_{c,i}}{\partial t}=\dot{m}_{c,i-1}c_{p,c}T_{c,i-1}-\dot{m}_{c,i}c_{p,c}T_{c,i}+\mathrm{h}_{cv,c,i}A_{cv,c,i}(T_{s,i}-T_{c,i}) \quad (1)$$

where, $\rho_{c,i}$ is the gas density of the cathode in the i-th control volume, $c_{p,c}$ is the constant-pressure specific heat capacity of the cathode gas, A_c is the cathode flow cross-sectional area, $T_{c,i}$ is the cathode gas temperature of the i-th control volume, $\dot{m}_{c,i}$ is the cathode gas mass flow rate of the i-th control volume, $\mathrm{h}_{cv,c,i}$ is the convective heat transfer coefficient between the cathode gas and the solid phase, $A_{cv,c,i}$ is the heat transfer area of the cathode in the i-th control volume, and $T_{s,i}$ is the solid-phase temperature of the stack in the i-th control volume. Through discretization, this equation enables the independent solution of the gas temperature in each control volume, accurately capturing temperature gradient variations along the flow direction, and overcoming the limitation of traditional lumped parameter models that cannot characterize local thermodynamic characteristics. The solid-phase energy equation embeds electrochemical reaction heat and ohmic heat terms to achieve deep coupling of electrochemical and thermodynamic processes, expressed as:

$$m_{s,i}c_{p,s}\frac{\partial T_{s,i}}{\partial t}=\mathrm{h}_{cv,c,i}A_{cv,c,i}(T_{c,i}-T_{s,i})+\mathrm{h}_{cv,a,i}A_{cv,a,i}(T_{a,i}-T_{s,i})+\dot{Q}_{rxn,i}+\dot{Q}_{ohm,i} \quad (2)$$

where, $m_{s,i}$ is the solid-phase mass of the stack in the i-th control volume, $c_{p,s}$ is the constant-pressure specific heat capacity of the solid phase, $T_{a,i}$ is the anode gas temperature of the i-th control volume, $\dot{Q}_{rxn,i}$ is the electrochemical reaction heat of the i-th control volume, and $\dot{Q}_{ohm,i}$ is the ohmic heat loss of the i-th control volume. The embedding of reaction heat and ohmic heat enables accurate characterization of energy conversion and losses caused by electrochemical processes, clarifying the sources of thermodynamic irreversibility and providing a basis for subsequent entropy production rate calculations.

As an important support for thermodynamic modeling, the electrochemical sub-model adopts a semi-empirical form to balance modeling accuracy and computational efficiency, with emphasis on introducing local temperature dependence to improve model adaptability. The Nernst voltage, as the theoretical open-circuit voltage of the stack, is calculated considering the local solid-phase temperature and gas partial pressures of the i-th control volume, expressed as:

$$E_{Nernst,i}=\frac{RT_{s,i}}{2F}\ln\left(\frac{P_{H_2,i}P_{O_2,i}^{0.5}}{P_{H_2O,i}}\right) \quad (3)$$

where, R is the universal gas constant, F is Faraday's constant, $P_{H2,i}$, $P_{O,i}$, $P_{H2O,i}$ are the partial pressures of hydrogen, oxygen, and water vapor in the i-th control volume, respectively. The activation overpotential is calculated based on the double polarization theory, embedding the local solid-phase temperature to reflect the effect of temperature on reaction kinetics, expressed as:

$$\eta_{act,i}=\frac{RT_{s,i}}{2F}\left[\sinh^{-1}\left(\frac{j_i}{2j_{0,a,i}}\right)+\sinh^{-1}\left(\frac{j_i}{2j_{0,c,i}}\right)\right] \tag{4}$$

where, j_i is the current density of the i-th control volume, $j_{0,a,i}$ and $j_{0,c,i}$ are the exchange current densities of the anode and cathode in the i-th control volume, respectively. Combining ohmic overpotential and concentration overpotential, the unit voltage of the i-th control volume can be expressed as:

$$V_i=E_{Nernst,i}-\eta_{act,i}-\eta_{ohm,i}-\eta_{conc,i} \tag{5}$$

where, $\eta_{ohm,i}$ is the ohmic overpotential of the i-th control volume, and $\eta_{conc,i}$ is the concentration overpotential of the i-th control volume. The introduction of local temperature dependence enables the electrochemical model to accurately match the thermodynamic state of each control volume, avoiding the prediction deviation caused by the use of average temperature in traditional models, and further improving the overall accuracy of thermodynamic modeling.

The model is solved using the Crank–Nicolson implicit time-marching scheme, which combines stability and computational accuracy and can effectively capture the thermal relaxation process of the stack. Considering that the system thermal time constant is 10–100 s, the time step is set to 0.1–1 s to ensure accurate tracking of the dynamic evolution of thermodynamic characteristics. During numerical solving, the finite difference method is used to discretize the governing equations, and matrix solving is employed to update parameters such as temperature and voltage in each control volume simultaneously, significantly improving computational efficiency. Tests show that the single-step solution time of the model is less than 10 ms. Compared with the minute-level solution time of traditional three-dimensional CFD models, the computational efficiency is improved by two orders of magnitude. It not only retains the ability to accurately capture key thermodynamic characteristics such as temperature gradients but also meets the real-time requirements of online state detection, achieving an effective balance between modeling accuracy and computational efficiency.

2.2 Entropy production rate decomposition and evolution characterization

Based on the temperature, current density, and overpotential distributions solved by the hybrid-dimensional thermodynamic dynamic model established above, combined with the fundamental theory of nonequilibrium thermodynamics, various types of irreversible losses within the system can be quantitatively evaluated. Figure 2 illustrates the decomposition of the SOFC "entropy fingerprint" and its correlation mechanism with multi-source measurable variables. According to the physical formation mechanisms of energy dissipation, the total entropy production rate across the entire fuel cell domain is divided into four mutually independent components, corresponding respectively to the electrochemical reaction activation process, charge transport process, species diffusion and mass transfer process, and gas–solid interface heat transfer process, thus completely covering all irreversible thermodynamic behaviors during system operation. The total entropy production rate of the system can be uniformly expressed as:

$$\dot{S}_{gen}=\dot{S}_{act}+\dot{S}_{ohm}+\dot{S}_{conc}+\dot{S}_{therm} \tag{6}$$

In this equation, $\dot{S}_{gen}$ is the total entropy production rate of the whole system, $\dot{S}_{act}$ is the entropy production rate due to electrochemical reaction activation, $\dot{S}_{ohm}$ is the entropy production rate caused by charge transport (ohmic loss), $\dot{S}_{conc}$ is the entropy production rate arising from species mass transfer (concentration overpotential), and $\dot{S}_{therm}$ is the entropy production rate due to gas–solid heat conduction. This decomposition strictly follows the local entropy balance criterion and enables segment-by-segment statistics of irreversible losses along the flow direction. Compared with global averaging calculation forms, it can accurately restore the spatial distribution pattern of entropy production inside the stack.

On the basis of clarifying the entropy production component division, explicit mathematical relationships between each entropy production component and the system's measured operating parameters are established, realizing the direct coupling of thermodynamic loss indicators with engineering-measurable physical quantities. The ohmic entropy production rate generated in the charge transport process takes the discrete control volume as the calculation unit, fully considering local temperature and current distribution differences. Its calculation expression is:

$$\dot{S}_{ohm}=\sum_{i=1}^{N}\frac{j_i^2A_iR_{ohm,i}}{T_{s,i}} \tag{7}$$

In practical engineering applications, the equivalent global ohmic resistance can be obtained via electrochemical impedance spectroscopy testing, and simplified solutions can be completed by combining the average solid-phase temperature, namely:

$$\dot{S}_{ohm}\approx\frac{I^2R_{ohm}}{T_{avg}} \tag{8}$$

where, N is the total number of discrete control volumes along the flow direction of the stack, j_i is the local current density of the i-th control volume, A_i is the effective reaction area of the corresponding control volume, $R_{ohm,i}$ is the equivalent ohmic impedance of the local region, $T_{s,i}$ is the solid-phase operating temperature of the control volume, I is the total output current of the stack, R_{ohm} is the global equivalent ohmic resistance of the stack, and T_{avg} is the average solid-phase temperature of the stack.

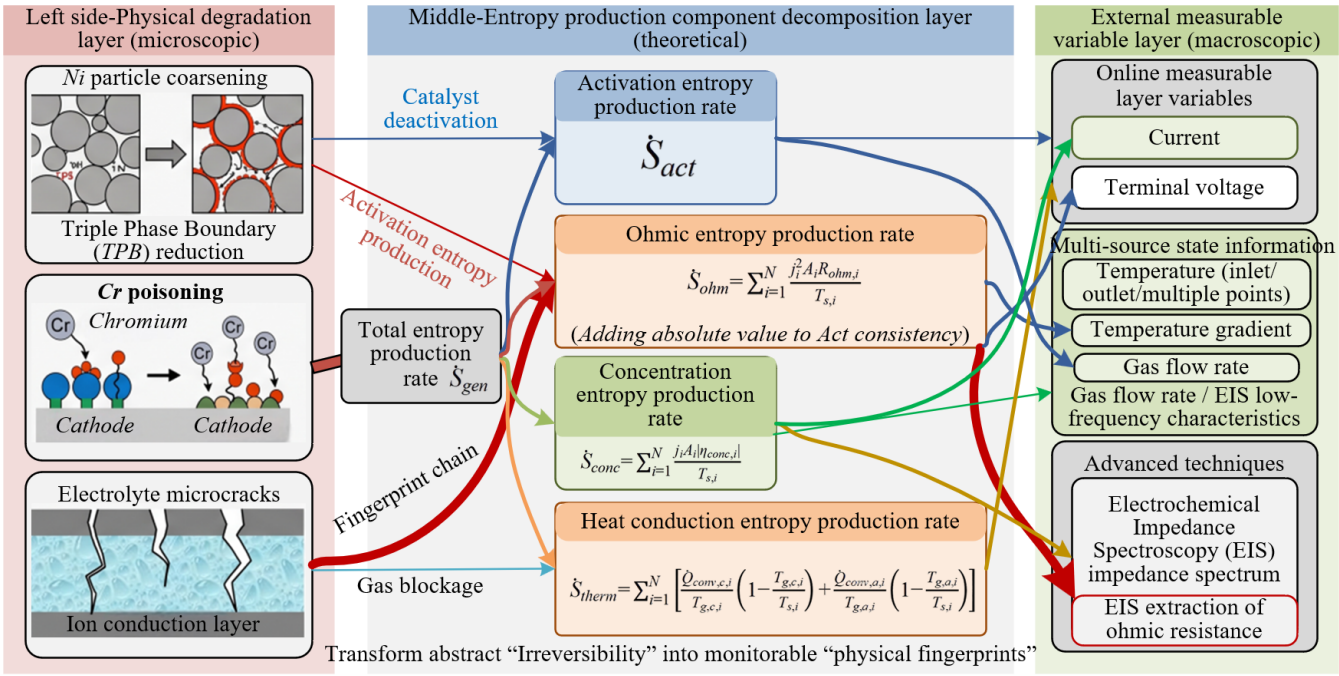

Figure 2. Mechanism diagram of Solid oxide fuel cell (SOFC) "entropy fingerprint" decomposition and correlation with multi-source measurable variables

The concentration entropy production rate caused by species mass transfer is jointly determined by the local current density and concentration polarization loss, and can be directly linked to inlet flow rate and composition concentration regulation parameters. Its expression is:

$$\dot{S}_{conc}=\sum_{i=1}^{N}\frac{j_i A_i|\eta_{conc,i}|}{T_{s,i}} \tag{9}$$

where, $\eta_{conc,i}$ is the concentration polarization overpotential inside the i-th control volume. The thermal conduction entropy production rate formed by the temperature difference between the gas and solid phases is solved using distributed temperature acquisition data, fully accounting for the irreversible heat loss caused by convection heat transfer at the anode and cathode sides. Its specific form is:

$$\dot{S}_{therm}=\sum_{i=1}^{N}\left[\frac{\dot{Q}_{conv,c,i}}{T_{g,c,i}}\left(1-\frac{T_{g,c,i}}{T_{s,i}}\right)+\frac{\dot{Q}_{conv,a,i}}{T_{g,a,i}}\left(1-\frac{T_{g,a,i}}{T_{s,i}}\right)\right] \tag{10}$$

where, $\dot{Q}_{conv,c,i}$ and $\dot{Q}_{conv,a,i}$ are the convective heat transfer quantities on the cathode and anode sides, respectively; $T_{g,c,i}$ and $T_{g,a,i}$ are the temperatures of the cathode and anode gas media, respectively. Through the above correlation forms, entropy production parameters that originally could only be solved offline using mechanism models can now be calculated in real time using conventional on-site monitoring equipment, greatly improving the engineering practicability of thermodynamic loss analysis.

Under different operating conditions, the proportion levels and variation trends of various entropy production components exhibit significantly differentiated characteristics. During the start-up heating stage, the large temperature difference between gas and solid makes heat conduction–related entropy production dominant. During rapid load switching, sudden changes in current density simultaneously cause fluctuations in ohmic loss and mass transfer loss. In the process of long-term continuous operation, material aging and structural degradation promote persistent unidirectional changes in specific types of entropy production. Slowly increasing electrolyte internal impedance continuously raises the overall proportion of ohmic entropy production, decreasing electrode catalytic activity steadily increases activation entropy production, and dust deposition and clogging in fuel channels directly aggravate irreversible mass transfer losses. By relying on long-term operational data statistics to analyze the composition ratio and time-series fluctuation patterns of various entropy production components, unique system operational characteristic patterns can be formed to distinguish different internal degradation forms and complete refined identification of the system's internal health status.

The state characterization system formed based on temporal evolution laws can effectively fill the lag problem in discrimination inherent in traditional external characteristic monitoring methods. When the fuel cell output voltage shows obvious decay, the internal irreversible losses of the system are often already at a relatively advanced stage, whereas directional shifts in entropy production components can capture internal degradation trends in advance before obvious changes occur in the macro electrical characteristics of the equipment. With this characterization method, normal operating intervals and abnormal degradation intervals can be clearly defined, while precisely distinguishing single-degradation types from compound-degradation conditions. This provides comprehensive, physically supported feature evidence for the subsequent construction of nonlinear state observation models and early operational anomaly warning.

2.3 Design of entropy production observer based on square-root unscented Kalman filter

The entropy production rate and its components, as core indicators characterizing the irreversible evolution of SOFC systems, cannot be directly measured by existing test equipment and require the construction of a nonlinear observer

to realize soft measurement. The strong nonlinear characteristics present during system operation make traditional linear observers prone to errors introduced by linearization approximations, leading to divergent estimation results and making it difficult to meet the requirements of high-precision online monitoring. To address this, an entropy production observer based on the SR-UKF is constructed. Through state-space modeling and multi-source data fusion, stable and accurate estimation of entropy production rates and their components is achieved. Figure 3 shows the flowchart of the nonlinear entropy production observer and fault detection based on the dual time-scale SR-UKF.

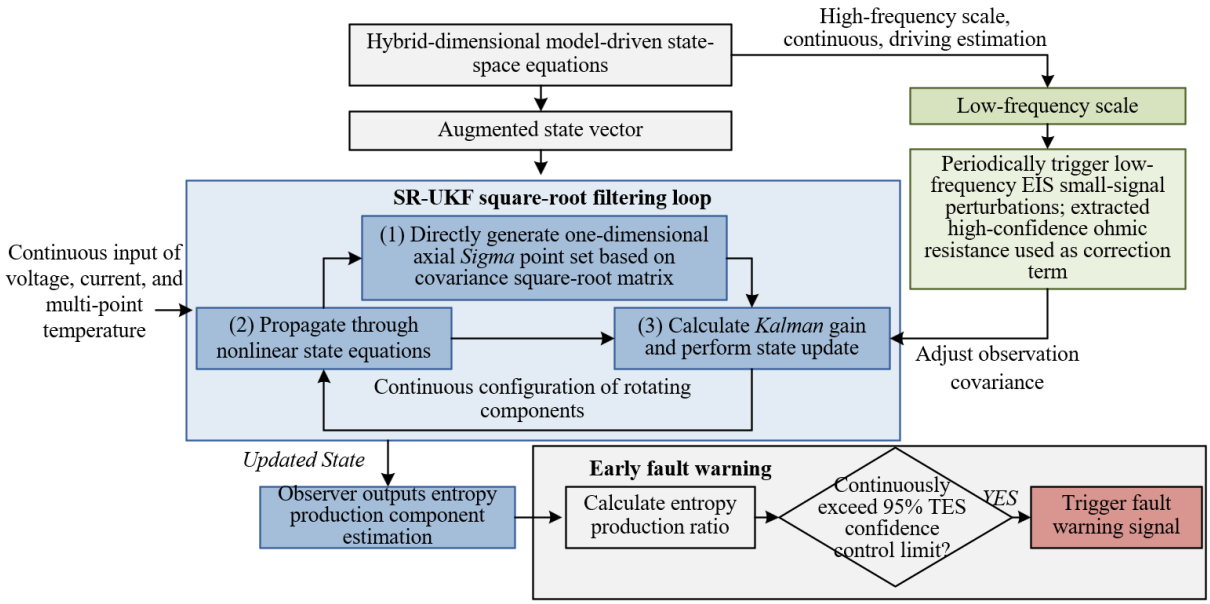

Figure 3. Flowchart of the nonlinear entropy production observer and fault detection based on the dual time-scale Square-Root Unscented Kalman Filter (SR-UKF)

The construction of the state-space model is based on the system's thermodynamic and electrochemical characteristics, with a focus on incorporating entropy production–related variables into the state vector to enable direct real-time estimation of irreversibility. The state equation and observation equation are expressed as:

$$x_{k+1}=f(x_k,u_k,\theta_k)+w_k \tag{11}$$

$$y_k=h(x_k,u_k)+v_k \tag{12}$$

where, x_k is the state vector at time step k, containing the total entropy production rate, individual entropy production components, solid-phase temperatures of each stack control volume, anode/cathode gas partial pressures, and key degradation parameters, thus comprehensively covering the thermodynamic and health states of the system; u_k is the input vector, including controllable operating parameters such as inlet flow rates, current load, and ambient temperature; θ_k is the model parameter vector; w_k is the process noise, following a Gaussian distribution with mean 0 and covariance Q; y_k is the observation vector, composed of measurable parameters such as voltage, current, and temperatures at monitoring points; and v_k is the observation noise, following a Gaussian distribution with mean 0 and covariance R. Incorporating entropy production variables directly into the state vector breaks the limitation of traditional observers that can only estimate macroscopic parameters, enabling direct tracking of irreversible evolution processes.

The observer adopts the SR-UKF algorithm, optimizing the covariance matrix update process through square-root decomposition to enhance numerical stability while reducing computational complexity. The core steps of the algorithm begin with Sigma point generation. Based on the state estimate and the square root of the covariance matrix, a set of Sigma points is generated to represent the probability distribution of the state vector, specifically:

$$X^{(0)}=\hat{x}_{k|k},\ W^{(0)}=\frac{\kappa}{n_x+\kappa} \tag{13}$$

$$X^{(j)}=\hat{x}_{k|k}\pm\left(\sqrt{(n_x+\kappa)P_{k|k}}\right)_j,\ W^{(j)}=\frac{1}{2(n_x+\kappa)} \tag{14}$$

where, $\hat{x}_{k|k}$ is the state estimate at time k, $P_{k|k}$ is the state estimation covariance matrix at time k, n_x is the dimension of the state vector, κ is a scaling factor chosen as 3-n_x to ensure numerical stability, and $W^{(j)}$ is the weight of the Sigma point. State prediction is performed through the nonlinear propagation of Sigma points, with the prediction given by:

$$\hat{x}_{k+1|k}=\sum_{j=0}^{2n_x} W^{(j)}\,X^{(j)}_{k+1|k} \tag{15}$$

In the observation update stage, the deviation between the observed value and the predicted observation is calculated, the Kalman gain is solved, and the state estimate and covariance matrix are updated. The Kalman gain is expressed as:

$$K_{k+1}=P_{xy}P_{yy}^{-1} \tag{16}$$

where, P_{xy} is the cross-covariance matrix between the state prediction and the observation prediction, and P_{yy} is the covariance matrix of the observation prediction. The introduction of square-root decomposition effectively prevents the covariance matrix from becoming non-positive definite, adapts to the strong nonlinearity of the system, and

solves the divergence problem common in traditional linear observers.

A dual time-scale data fusion strategy is adopted to improve observation accuracy, realizing an organic combination of high-frequency real-time tracking and low-frequency precise calibration. At the high-frequency level, conventional monitoring data such as voltage, current, and temperature are collected every second, and the observer estimates the entropy production rate in real time, ensuring the timeliness of online monitoring. At the low-frequency level, electrochemical impedance spectroscopy tests are triggered every 5–30 minutes to extract the system's equivalent ohmic resistance, which is then used to calibrate the estimated results of the ohmic entropy production rate. The measurement uncertainty of the electrochemical impedance spectroscopy test is controlled within ±2%, and the covariance R_{EIS} for the calibration process is set accordingly to ensure calibration accuracy. Based on the observed entropy production components, entropy production ratio indicators are defined for fault detection. Taking the ohmic entropy production ratio as an example, its expression is:

$$r_{ohm}=\frac{\dot{S}_{ohm}}{\dot{S}_{ohm,0}} \tag{17}$$

where, $\dot{S}_{ohm,0}$ is the baseline value of the ohmic entropy production rate during the initial normal operation period. The 95% confidence interval for each entropy production ratio is determined through statistical analysis, and the control limit is set to 1.3. When a certain entropy production ratio exceeds the control limit, the system is judged to have experienced corresponding type of degradation or fault, and an early warning signal is issued, realizing precise monitoring and anomaly warning of the system's operational state.

2.4 Physics-informed neural network-assisted hybrid degradation model

Although the thermodynamic mechanism model established earlier can fully reproduce the entropy production evolution law of the fuel cell under conventional operating conditions, it is difficult to achieve high-precision characterization for complex degradation behaviors involving the coupling of multiple factors such as electrode microstructure evolution and interface impurity poisoning, relying solely on physical equations. Pure data-driven models, despite having strong data-fitting capabilities, tend to deviate from basic thermodynamic principles, and their inference results are prone to unreasonable phenomena that violate the laws of energy conservation and entropy increase. Therefore, a hybrid degradation modeling framework combining mechanism models and physics-informed neural networks is constructed. The deterministic thermodynamic mechanism model is used to build the main framework of system loss evolution, and the neural network is employed to compensate for modeling deviations caused by complex degradation processes, effectively solving the state prediction problem under the condition of scarce measured time-series degradation data samples. Figure 4 shows the topology of the Physics-Informed Neural Network (PINN)-assisted hybrid degradation model embedded with thermodynamic hard constraints.

The physics-informed neural network constructed in this paper takes the system's actual operating conditions and time-series information as input features. After multi-layer nonlinear mapping operations, it outputs entropy production deviation corrections, which are used for dynamic correction of the mechanism model's solution results. The network training process no longer relies solely on measured data for fitting; instead, the fundamental laws of thermodynamics are embedded into the loss function to complete joint constrained training. The overall loss function is constructed as follows:

$$L=L_{data}+\lambda_1\left(1-\frac{\sum_k(\dot{S}_{k,mech}+\Delta\dot{S}_k)}{\sum_k\dot{S}_{k,mech}+\sum_k\Delta\dot{S}_k}\right)^2+\lambda_2\sum_k\max(0,-\Delta\dot{S}_k)^2 \tag{18}$$

The first term is the measured data fitting loss, used to reduce the deviation between the model calculation results and the actual observation data; the second term is the global entropy increase constraint, ensuring that the total entropy production change trend of the system over the entire time range conforms to the basic laws of irreversible process thermodynamics; the third term is the non-negative constraint for each entropy production component, preventing corrected loss entropy production from taking negative values or other physically unrealistic calculation results. Parameters and are the weighting coefficients of the two physical constraints, which can be adaptively adjusted according to operating condition characteristics and model fitting requirements, ensuring data fitting accuracy while firmly maintaining the boundaries of physical mechanisms.

After completing network training, the correction output by the neural network is coupled and superimposed with the calculated values of the mechanism model to obtain real-time entropy production results that take into account both physical laws and actual degradation characteristics. The fusion expression is:

$$\dot{S}_{gen,total}=\dot{S}_{gen,mech}+N_{PINN}(z_k) \tag{19}$$

where, z_k represents the set of input features of the current operating condition, and $N_{PINN}(z_k)$ is the entropy production correction vector output by the physics-informed neural network. During the operation of the entire detection system, this hybrid model is embedded into the state prediction step of the SR-UKF, and the corrected entropy production sequence is used to optimize the prior state estimation results, alleviating the prediction drift problem of a single mechanism model under long-term aging conditions, and further enhancing the state tracking capability of the observer in slow-varying degradation scenarios.

This hybrid modeling form realizes the deep integration of theoretical mechanisms and measured information, preserving both the clear physical logic and interpretability of traditional thermodynamic models—consistent with academic research norms in energy and thermodynamic system modeling—and fully leveraging the ability of data-driven methods to uncover hidden degradation patterns. Even in scenarios where only a small amount of valid labeled data remains after long-term continuous operation, the built-in physical constraints still ensure the rationality of the model inference results, further completing the full theoretical system from thermodynamic characteristic evolution analysis to online operational state detection.

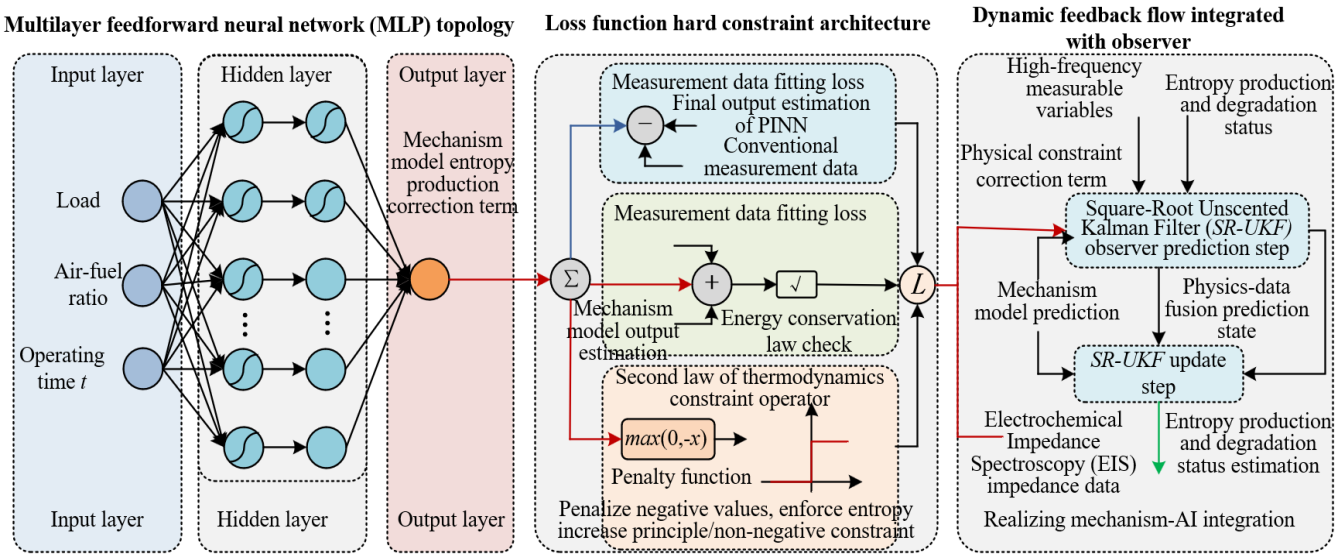

Figure 4. Topology of the Physics-Informed Neural Network (PINN)-assisted hybrid degradation model embedded with thermodynamic hard constraints

3. EXPERIMENTAL VALIDATION

3.1 Experimental platform and test scheme

The experiment uses a 500 W SOFC single stack to build the test platform. The electrolyte is yttria-stabilized zirconia, the anode material is nickel–yttria-stabilized zirconia cermet, the cathode material is lanthanum strontium manganite, and the effective area of the stack is 100 cm². The platform is equipped with a complete auxiliary system, including a fuel supply module, an oxidant supply module, a temperature control module, and a data acquisition module. Hydrogen is used as the fuel, air as the oxidant, and the inlet gas parameters are precisely regulated by mass flow controllers. Measurement equipment includes K-type thermocouples (measurement accuracy ±0.5 K), high-precision current/voltage sensors (measurement accuracy ±0.1%), an electrochemical impedance spectroscopy tester (test frequency range 10 mHz–1 MHz, measurement accuracy ±2%), and a gas analyzer (measurement accuracy ±0.1%). The sampling frequency for all data is set to 1 Hz to ensure the capture of system dynamic operating characteristics.

The experiment is designed around the core objectives of thermodynamic characteristic evolution and operational state detection for SOFC systems, covering typical operating conditions such as startup, load change, and aging. Multiple comparative experiments are conducted to verify the accuracy, computational efficiency, and fault warning capability of the proposed innovative methods, while traditional models and methods are set as controls to highlight the superiority of the proposed approaches. All experiments are carried out under standard environmental conditions (ambient temperature 25 °C, atmospheric pressure 101.325 kPa). Before testing, the stack is activated to ensure stable performance.

3.2 Accuracy and efficiency verification experiment of the hybrid-dimensional model

This experiment aims to verify the accuracy and computational efficiency advantages of the proposed hybrid-dimensional thermodynamic dynamic model compared with the three-dimensional CFD model and the traditional lumped parameter model. A steady-state condition is set, with the current density ranging from 0.3 to 0.8 A/cm², and test points are arranged at intervals of 0.1 A/cm². Each test point operates stably for 30 minutes, measuring the temperature at five characteristic points along the flow direction of the stack and the stack voltage. The prediction results of the three models are compared, and the single-step solution time of each model is recorded. The experimental evaluation indicators include the root mean square error (RMSE) of temperature prediction, the RMSE of voltage prediction, and the single-step solution time. The experimental data are shown in Table 1.

From the data in Table 1, it can be seen that the hybrid-dimensional model has an average temperature prediction RMSE of 2.3 K and a voltage prediction RMSE of 0.9%, with a single-step solution time of 8.6 ms. Its accuracy is close to that of the 3D CFD model (average temperature RMSE 1.8 K, voltage prediction RMSE 0.7%), but its computational efficiency is improved by two orders of magnitude compared with the 3D CFD model, solving the problem that the 3D CFD model is computationally cumbersome and unable to meet online application requirements. Although the traditional lumped parameter model has the shortest single-step solution time (6.2 ms), its temperature prediction RMSE reaches 8.5 K and its voltage prediction RMSE is 3.2%. It cannot capture the temperature gradient along the flow direction of the stack, showing large deviations from the actual thermodynamic characteristics and making it difficult to support high-precision state detection. Through the architectural design of one-dimensional discretization of the stack and zero-dimensional lumping of the auxiliary system, the hybrid-dimensional model achieves an effective balance between modeling accuracy and computational efficiency, fully meeting the requirements of online operation.

3.3 Entropy production evolution characteristics verification experiment

This experiment aims to verify the accuracy of the entropy production decomposition model and confirm the correspondence between entropy fingerprints and degradation

modes. The experiment is divided into three sub-conditions: startup, load step change, and simulated degradation. The startup condition involves heating from room temperature to 800 °C at a heating rate of 5 °C/min. The load step condition sets the current density sequentially to 0.4 → 0.6 → 0.3 A/cm², with each load maintained stably for 20 min. For the simulated degradation condition, two degradation modes—electrolyte aging and fuel channel blockage—are artificially introduced, with each degradation mode running for 100 h. Temperature, current, voltage, and gas composition data are measured under each condition, and the experimental and model-predicted values of entropy production components are calculated to verify the accuracy of the entropy production decomposition model and the effectiveness of the entropy fingerprint. The experimental data are shown in Tables 2 and 3.

From the data in Table 2, it can be seen that under startup and load step conditions, the average prediction error of entropy production components is below 3.2%. Specifically, the prediction error for activation entropy production is 2.4%–2.9%, for ohmic entropy production 2.1%–2.5%, for concentration entropy production 2.6%–3.1%, and for heat conduction entropy production 2.5%–2.9%, verifying the accuracy of the entropy production decomposition model and its ability to precisely quantify the entropy contribution of each irreversible process. From the data in Table 3, it can be seen that during electrolyte aging, the proportion of ohmic entropy production gradually increases from the initial 28.6% to 42.3%, an increase of 47.9%, far exceeding the changes in other entropy production components. During fuel channel blockage, the proportion of concentration entropy production increases from the initial 24.2% to 38.1%, an increase of 57.4%. The changes in entropy production component proportions under the two degradation modes exhibit significantly differentiated characteristics, which are fully consistent with the definition of the entropy fingerprint, proving that the entropy fingerprint can accurately characterize different degradation modes and provide a reliable thermodynamic basis for early system fault localization.

Table 1. Experimental data comparing the accuracy and efficiency of the three models

Current Density /($A \cdot cm^{-2}$)	Measured Temperature / K	Hybrid-Dimensional Model		3D Computational Fluid Dynamics (CFD) Model		Traditional Lumped Parameter Model	
		Prediction Temperature / K	Root Mean Square Error $(RMSE)$ / K	Prediction Temperature / K	$RMSE/K$	Prediction Temperature / K	$RMSE/K$
0.3	723.5	725.1	2.3	724.1	1.8	731.8	8.3
0.4	741.2	743	2.2	742.5	1.9	749.7	8.5
0.5	758.7	760.8	2.4	759.9	1.8	767.2	8.4
0.6	776.3	778.5	2.3	777.4	1.7	784.9	8.6
0.7	793.8	796	2.2	795.1	1.9	802.6	8.8
0.8	811.4	813.5	2.3	812.6	1.8	820.2	8.7
Average Temperature $RMSE/K$	-	-	2.3	-	1.8	-	8.5
Voltage Prediction $RMSE$/%	-	-	0.9	-	0.7	-	3.2
Single-Step Solution Time /ms	-	-	8.6	-	1250	-	6.2

Table 2. Prediction error data of entropy production components under startup and load step conditions

Operating Condition Type	Operating Time / min	Total Entropy Production Rate / ($W \cdot K^{-1}$)	Activation Entropy Production Prediction Error / %	Ohmic Entropy Production Prediction Error / %	Concentration Entropy Production Prediction Error / %	Heat Conduction Entropy Production Prediction Error / %	Average Prediction Error / %
Startup condition	10	0.125	2.8	2.5	3.1	2.9	2.8
Startup condition	30	0.186	2.6	2.3	2.9	2.7	2.6
Startup condition	50	0.218	2.5	2.2	2.7	2.6	2.5
Startup condition	70	0.232	2.4	2.1	2.6	2.5	2.4
Load step condition	20(0.4A/cm^2)	0.205	2.7	2.3	2.8	2.6	2.6
Load step condition	40(0.6A/cm^2)	0.278	2.9	2.4	3	2.8	2.8
Load step condition	60(0.3A/cm^2)	0.182	2.6	2.2	2.7	2.5	2.5

Table 3. Variation data of entropy production component proportions under simulated degradation conditions

Degradation Mode	Operating Time / h	Total Entropy Production Rate / ($W \cdot K^{-1}$)	Activation Entropy Production Proportion / %	Ohmic Entropy Production Proportion / %	Concentration Entropy Production Proportion / %	Heat Conduction Entropy Production Proportion / %
Normal condition	0	0.203	32.5	28.6	24.2	14.7
Electrolyte aging	20	0.215	32.8	33.1	23.9	10.2
Electrolyte aging	60	0.231	33	38.5	23.7	4.8
Electrolyte aging	100	0.248	33.2	42.3	23.5	1
Fuel channel blockage	20	0.218	32.6	28.8	28.9	9.7
Fuel channel blockage	60	0.235	32.7	29.1	34.5	3.7
Fuel channel blockage	100	0.252	32.9	29.3	38.1	0.7

3.4 State detection accuracy verification experiment

This experiment aims to verify the entropy production estimation accuracy of the SR-UKF-based entropy production observer, comparing its performance with the traditional Extended Kalman Filter (EKF) observer and the voltage monitoring method. Both normal and mild degradation conditions (degradation degree < 5%) are set, each running stably for 80 h. The SR-UKF and EKF observers are used to estimate the entropy production rate, and the experimental entropy production rate is indirectly calculated for comparison. The entropy production estimation RMSE, fault warning time, and observer stability of the three methods are compared. The experimental data are shown in Table 4.

From the data in Table 4, it can be seen that under normal conditions, the entropy production estimation RMSE of the SR-UKF observer is 2.8%, significantly lower than the 8.2% of the EKF observer, and the operation is stable without divergence. Under mild degradation conditions, the entropy production estimation RMSE of the SR-UKF observer is 3.1%, still maintaining high accuracy, with a fault warning time of 42 min. In contrast, the entropy production estimation RMSE of the EKF observer rises to 8.7%, and estimation divergence occurs in the later stage of operation, with a fault warning time of only 34 min, which is 19.0% shorter than that of the SR-UKF observer. The traditional voltage monitoring method detects no abnormal signals under mild degradation conditions and cannot achieve early warning, highlighting the superiority of the entropy-production-rate-based state detection method. By optimizing the covariance matrix update process through square-root decomposition, the SR-UKF observer effectively adapts to the strong nonlinear characteristics of the system, solves the divergence problem caused by linearization errors in the traditional EKF observer, and achieves accurate and stable estimation of entropy production rates. At the same time, it captures system degradation trends in advance, providing effective support for early fault warning.

3.5 Verification experiment of electrochemical impedance spectroscopy-assisted calibration effectiveness

This experiment aims to verify the improvement effect of Electrochemical Impedance Spectroscopy (EIS) calibration on entropy production estimation accuracy within the dual time-scale data fusion strategy. Two comparative experiments are set up: the experimental group uses the SR-UKF observer with EIS calibration, and the control group uses the SR-UKF observer based only on voltage, temperature, and current. Both groups run under aging conditions for 200 h, and the entropy production estimation RMSE is recorded every 20 h to statistically analyze the long-term operational accuracy attenuation. The experimental data are shown in Table 5.

From the data in Table 5, it can be seen that as operating time increases, the entropy production estimation RMSE of both observers gradually increases, but the growth rate of the experimental group is significantly lower than that of the control group. After 200 h of operation, the entropy production estimation RMSE of the experimental group is 3.3%, with an accuracy attenuation of only 0.5%, while that of the control group rises to 5.2%, with an accuracy attenuation of 2.3%. The entropy production estimation RMSE of the experimental group is 36.5% lower than that of the control group, and the long-term operational stability is significantly improved. The EIS test can accurately extract the system's equivalent ohmic resistance, and the dual time-scale data fusion strategy calibrates the estimation result of the ohmic entropy production rate, effectively correcting the estimation deviation caused by parameter drift during long-term operation, improving the long-term operational accuracy and stability of the observer, and verifying the effectiveness of the dual time-scale data fusion strategy.

Table 4. Performance comparison data of three state detection methods

Operating Condition Type	Detection Method	Entropy Production Estimation Root Mean Square Error (RMSE) / %	Fault Warning Time / min	Observer Stability
Normal condition	Square-Root Unscented Kalman Filter (SR-UKF) observer	2.8	-	Stable
Normal condition	Extended Kalman Filter (EKF) observer	8.2	-	Basically stable
Normal condition	Voltage monitoring method	-	-	-
Mild degradation condition	SR-UKF observer	3.1	42	Stable
Mild degradation condition	EKF observer	8.7	34	Prone to divergence
Mild degradation condition	Voltage monitoring method	-	No warning	-

Table 5. Comparative experimental data on the effectiveness of Electrochemical Impedance Spectroscopy (EIS)-assisted calibration

Operating Time /*h*	Experimental Group (with EIS Calibration)		Control Group (Without EIS Calibration)	
	Entropy Production Estimation Root Mean Square Error (*RMSE*)/%	Accuracy Attenuation /%	Entropy Production Estimation *RMSE*/%	Accuracy Attenuation /%
0	2.8	0	2.9	0
40	2.9	0.1	3.2	0.3
80	3	0.2	3.6	0.7
120	3.1	0.3	4.1	1.2
160	3.2	0.4	4.7	1.8
200	3.3	0.5	5.2	2.3

3.6 Performance verification experiment of the PINN hybrid model

This experiment aims to verify the accuracy advantage of the PINN hybrid model compared with the pure mechanism model and the pure Neural Network (NN) model, especially under data-scarce scenarios. Two data scenarios are set: the sufficient data scenario (200 h aging data) and the scarce data scenario (50 h aging data). The pure mechanism model, pure NN model, and PINN hybrid model are trained separately, and the entropy production estimation RMSE and physical constraint satisfaction (entropy increase deviation) of the three models are compared. The experimental data are shown in Table 6.

From the data in Table 6, it can be seen that in the sufficient data scenario, the entropy production estimation RMSE of the PINN hybrid model is 2.7%, better than the 4.6% of the pure mechanism model and the 3.4% of the pure NN model. The entropy increase deviation is 0.4%, comparable to the pure mechanism model and much lower than the 3.2% of the pure NN model, indicating that the PINN hybrid model can improve modeling accuracy while ensuring physical consistency. In the scarce data scenario, the entropy production estimation RMSE of the PINN hybrid model only rises to 3.4%, with an entropy increase deviation of 0.5%, while that of the pure NN model surges to 7.2% with an entropy increase deviation of 3.5%, and the pure mechanism model rises to 5.1%. This highlights the advantage of the PINN hybrid model in data-scarce scenarios. By embedding thermodynamic laws as hard constraints into the neural network loss function, the PINN hybrid model effectively avoids the physically unreasonable results that violate physical laws in the pure NN model, while using the neural network to compensate for the modeling deviation of the pure mechanism model under complex degradation scenarios, achieving a balance between physical consistency and modeling accuracy. It is especially suitable for engineering practice with scarce labeled data.

To quantitatively verify the effectiveness of the unified entropy production rate characterization framework in state detection under load disturbance, degradation identification, and long-term aging conditions, this paper further conducts a dynamic visualization experiment. From Figure 5(a), it can be seen that when the current density jumps from 0.3 A/cm² to 0.6 A/cm² at 20 min, the total entropy production rate rapidly increases from about 0.33 $W \cdot K^{-1}$ to about 1.34 $W \cdot K^{-1}$, an increase of about 306%, indicating that load increase significantly amplifies the total irreversible loss of the system. Among them, the ohmic entropy production rate increases from about 0.26 $W \cdot K^{-1}$ to about 0.84 $W \cdot K^{-1}$, being the first component to respond, indicating that the increase in current first strengthens the electrolyte resistance and electrode ohmic loss, while the concentration entropy production rate gradually increases from about 0.17 $W \cdot K^{-1}$ to about 0.70 $W \cdot K^{-1}$, with a response lag of about 5 to 10 min, reflecting a noticeable mass transfer delay in the gas diffusion and fuel supply process. After the load decreases at 50 min, the total entropy production rate falls back to about 0.60 $W \cdot K^{-1}$, but the heat conduction entropy production rate briefly rises from about 0.10 $W \cdot K^{-1}$ to about 0.18 $W \cdot K^{-1}$, indicating that the inertia of the temperature field causes thermal irreversible processes to be asynchronous with electrochemical load changes. Figure 5(b) further shows that in the electrolyte aging trajectory, the proportion of ohmic entropy production increases from 28.6% to 42.3%, a relative increase of about 47.9%, while the proportion of concentration entropy production remains basically around 24%, indicating that this degradation mainly manifests as increased ion conduction impedance. In the fuel channel blockage trajectory, the proportion of concentration entropy production increases from 24.2% to 38.1%, a relative increase of about 57.4%, while the proportion of ohmic entropy production only changes slightly to 29.3%. The two trajectories clearly deviate from the 95% confidence ellipse of normal operating conditions and separate in different directions, proving that the entropy fingerprint has the ability to distinguish degradation modes. Figure 5(c) shows that by 200 h of long-term operation, the deviation of the pure mechanism model gradually increases to about 8%–9%, exceeding the engineering acceptable threshold of ±5%; the pure NN model diverges after 50 h due to data scarcity, and the final deviation expands to about −12%. In contrast, the PINN hybrid model remains basically within ±3% throughout the entire lifespan and further suppresses drift after EIS calibration at 120 h. In summary, this figure uses dynamic response amplitude, component proportion migration, and long-term estimation deviation as quantitative evidence to prove that the entropy production rate can serve as a unified variable connecting the thermodynamic characteristic evolution and operational state detection of SOFC systems. The SR-UKF observer can reliably track transient irreversible processes, and the PINN hybrid model can maintain higher estimation stability under aging and data-scarce conditions, providing direct support for the thermodynamic characteristic evolution and state detection model proposed in this paper.

Table 6. Performance comparison data of the three models under different data scenarios

Data Scenario	Model Type	Entropy Production Estimation Root Mean Square Error (*RMSE*)/%	Entropy Increase Deviation /%
Sufficient data scenario	Physics-Informed Neural Network (PINN) hybrid model	2.7	0.4
Sufficient data scenario	Pure mechanism model	4.6	0.3
Sufficient data scenario	Pure Neural Network (NN) model	3.4	3.2
Scarce data scenario	PINN hybrid model	3.4	0.5
Scarce data scenario	Pure mechanism model	5.1	0.3
Scarce data scenario	Pure NN model	7.2	3.5

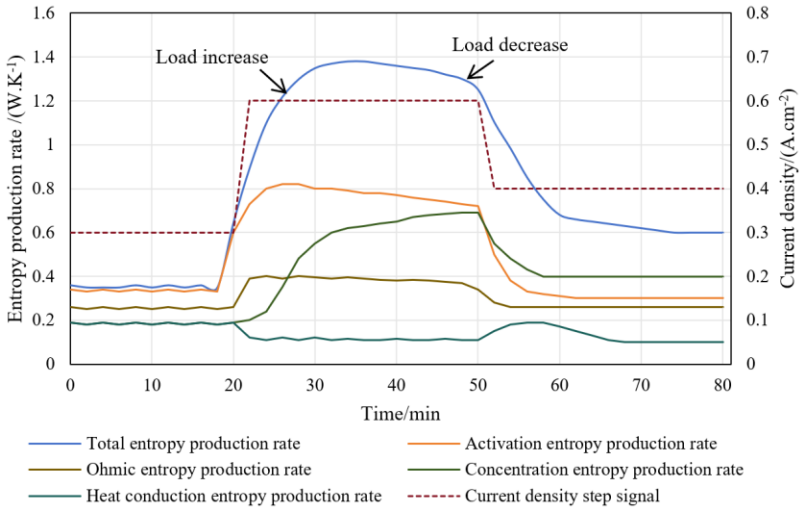

(a) Dynamic response curves of total entropy production rate and its components under load step conditions

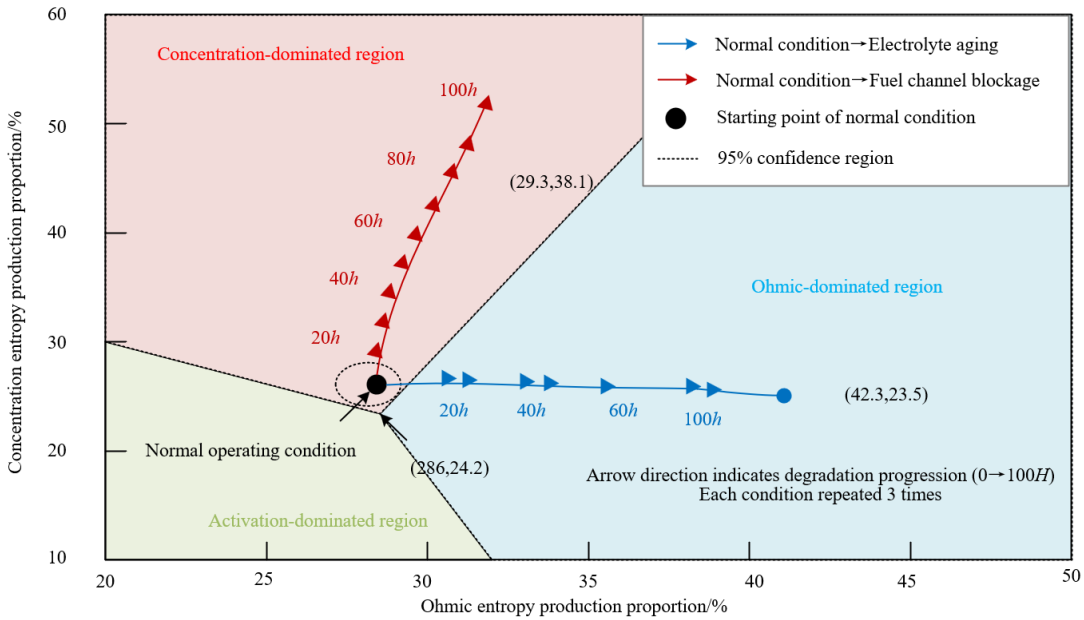

(b) Evolution trajectories of entropy fingerprints under different degradation modes

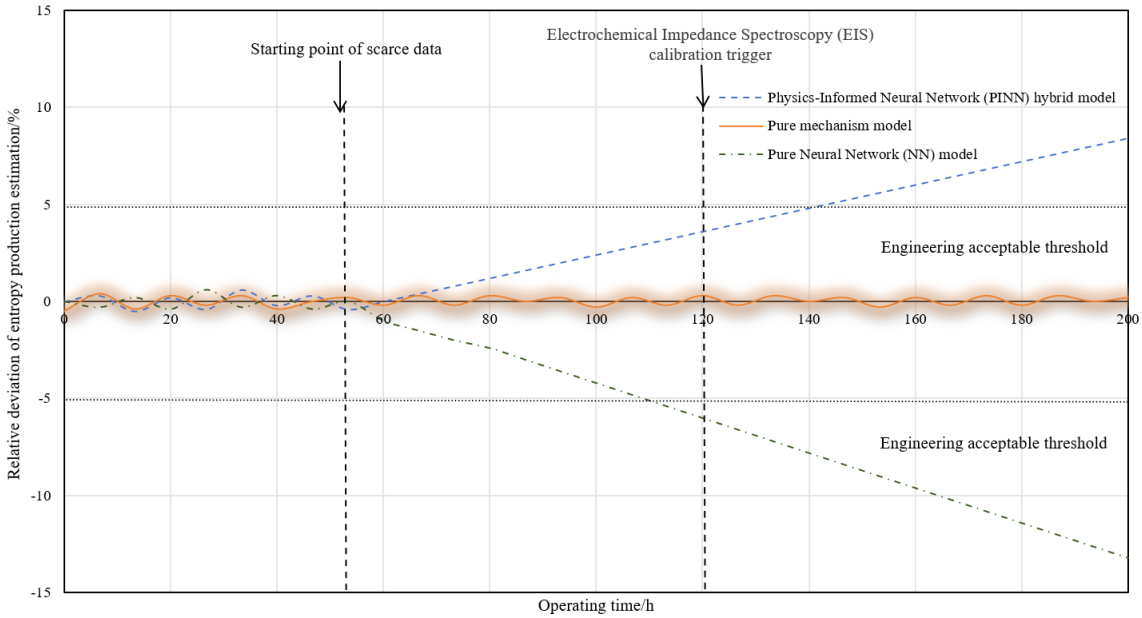

(c) Evolution of entropy production estimation deviation between the Physics-Informed Neural Network (PINN) hybrid model and the pure mechanism model during long-term aging

Figure 5. Entropy production component evolution and state detection response characteristics of a solid oxide fuel cell (SOFC) system under typical dynamic operating conditions

4. RESULTS AND DISCUSSION

The performance advantage of the hybrid-dimensional thermodynamic dynamic model originates from the high degree of alignment between its architectural design and the thermodynamic characteristics of SOFC systems. From the perspective of nonequilibrium thermodynamics, the distribution of irreversible entropy production inside the stack is mainly dominated by the temperature gradient along the flow direction. The one-dimensional discretization divides the stack into 8–12 control volumes, which can accurately capture the spatial distribution and dynamic evolution of the temperature gradient, providing a basis for precise calculation of the entropy production rate. The auxiliary system adopts zero-dimensional lumped modeling, following the approximation criteria of engineering thermodynamics. Its internal temperature gradient is much smaller than that of the stack, and the heat transfer process is dominated by the inlet–outlet temperature difference. Zero-dimensional modeling simplifies the computational structure without sacrificing core accuracy. Experimental results show that the model's temperature prediction RMSE is only 2.3 K, the voltage prediction RMSE is 0.9%, and the single-step solution time is 8.6 ms. Its accuracy is close to that of the three-dimensional CFD model, yet its computational efficiency is improved by two orders of magnitude, effectively resolving the accuracy–efficiency contradiction in traditional modeling methods. Compared with the minute-level solution time of the 3D CFD model, this model meets online operation requirements. In contrast, the traditional lumped parameter model cannot capture temperature gradients, resulting in a temperature prediction error as high as 8.5 K, making it difficult to support high-precision state detection, further highlighting the engineering practicality and thermodynamic rationality of the hybrid-dimensional architecture. Entropy production evolution analysis based on this model shows that entropy production components exhibit significantly differentiated characteristics under different operating conditions: during the startup stage, rapid temperature rise leads to significant gas–solid temperature differences, and heat conduction entropy production dominates, reflecting the strengthening of irreversible heat transfer processes; during the load change stage, sudden changes in current density cause drastic fluctuations in charge transport and mass transfer processes, with ohmic entropy production and concentration entropy production alternately dominating; during the aging stage, the directional shift of specific entropy production components essentially reflects the continuous strengthening of corresponding irreversible processes. The resulting entropy fingerprint can accurately characterize the root cause of degradation, providing a reliable thermodynamic basis for early fault localization, and realizing the direct link between irreversible evolution mechanisms and system health status.

The performance verification results of the state detection model and the PINN hybrid model further improve the integrated framework of thermodynamic characteristic evolution and online detection. The reason why the SR-UKF-based entropy production observer outperforms the traditional EKF observer lies in its square-root decomposition strategy, which adapts to the strong nonlinear thermodynamic characteristics of SOFC systems, avoids the non-positive-definite problem of the covariance matrix, and effectively solves the error and estimation divergence problems caused by EKF linearization approximations. In experiments, its entropy production estimation RMSE remains stable within 3.2%, and operation is stable. In the dual time-scale data fusion strategy, the thermodynamic value of EIS-assisted calibration is reflected in its ability to accurately extract ohmic resistance, directly linking it to charge transport irreversibility, and effectively correcting entropy production estimation deviations caused by parameter drift during long-term operation. This keeps the observer's long-term operational accuracy attenuation within 0.5%, significantly improving the stability of state detection. By embedding thermodynamic laws such as the entropy increase principle and non-negativity of components as hard constraints into the loss function, the PINN hybrid model fundamentally avoids the physical paradoxes common in pure data-driven models, ensuring that inference results conform to basic thermodynamic laws.

Although this study achieves precise management and control of thermodynamic characteristic evolution and operational state detection for SOFC systems, certain limitations remain. Experimental verification mainly focuses on conventional operating conditions, without fully considering entropy production evolution laws under extreme conditions such as extreme temperatures or high-load shocks. Under such conditions, multi-physics coupling effects are more complex and may cause fluctuations in model accuracy. At the same time, the training efficiency of the PINN still has room for improvement, as the complex network structure leads to long training times, making it difficult to adapt to fast-iterating engineering application scenarios. To address these limitations, multi-physics coupling theory can be introduced in future work to improve the entropy production calculation model under extreme conditions and enhance the model's generalization ability. By optimizing the PINN network structure and introducing lightweight training algorithms, the training cycle can be shortened and engineering practicality enhanced. Combining current research hotspots in thermodynamics and energy equipment, future studies can further explore the quantitative relationship between entropy production rate and SOFC lifetime, establishing a lifetime prediction model based on entropy production evolution; extend entropy production collaborative detection methods to multi-stack systems to achieve overall health management of multi-unit systems; and promote the further engineering application of nonequilibrium thermodynamics in complex energy systems, providing more comprehensive technical support for the commercialization of SOFCs.

5. CONCLUSION

Aiming at the performance degradation caused by the continuous evolution of thermodynamic characteristics during long-term operation of SOFCs, as well as the many shortcomings of existing state detection technologies, this paper establishes a complete integrated research framework covering mechanism analysis, state perception, and degradation identification. The hybrid-dimensional thermodynamic dynamic model constructed in this study effectively balances numerical simulation accuracy and online computation efficiency. Based on entropy production decomposition theory, it quantitatively distinguishes irreversible losses from different sources, realizes stable online estimation of entropy production parameters by combining the SR-UKF algorithm, and introduces a physics-informed neural network to achieve precise correction of

complex degradation behaviors. From the four aspects of modeling architecture, feature characterization, state observation, and deviation compensation, the long-standing technical difficulties in this field are resolved. By taking entropy production rate as the core bridge, this study connects the thermodynamic evolution laws with system health monitoring, improves the quantitative analysis system for irreversible processes in energy conversion equipment, and further consolidates the application foundation of nonequilibrium thermodynamics in the field of energy equipment operation and maintenance.

Extensive comparative experiments and multi-condition field measurements fully demonstrate that the proposed methods outperform traditional approaches in temperature and voltage prediction, dynamic entropy production estimation, and early anomaly warning. The overall model computation speed and detection accuracy meet the real-time monitoring requirements of engineering sites, and the evolution laws of internal thermodynamic behavior under different degradation modes can be accurately captured. The relevant research results can not only provide theoretical guidance for optimizing the operation strategy of SOFCs, but also offer reference research ideas and technical paradigms for the state assessment and lifetime management of similar high-temperature electrochemical energy devices.

REFERENCES

[1] Zhao, L.Q., Li, H., Jiang, N. Z., Hong, T.L., Mao, Y., Wang, Y.Y. (2025). Advances in waste heat recovery technologies for SOFC/GT hybrid systems. Power Engineering and Engineering Thermophysics, 4(1): 12-29. https://doi.org/10.56578/peet040102

[2] Lee, S., Oh, S., Lee, S., Jang, H. (2024). Development of an ammonia decomposition reactor, afterburner and post-decomposition reactor for 1 kW solid oxide fuel cells using ammonia. Energy Conversion and Management, 314: 118661. https://doi.org/10.1016/j.enconman.2024.118661

[3] Ilie, G. (2009). The opportunity of the investment in renewable energy capacities in the context of energy and financial crisis. Metalurgia International, 14(8): 25-28.

[4] Yokuş, T. (2024). Early warning systems for world energy crises. Sustainability, 16(6): 2284. https://doi.org/10.3390/su16062284

[5] Tang, Y., Liu, L., Li, Y., Wang, F. (2011). The electrochemical corrosion mechanisms of pure Cr with NaCl deposit in water vapor at 600℃. Journal of the Electrochemical Society, 158(8): C237-C241. https://doi.org/10.1149/1.3596167

[6] Tang, Y., Liu, L., Li, Y., Wang, F. (2010). Evidence for the occurrence of electrochemical reactions and their interaction with chemical reactions during the corrosion of pure Fe with solid NaCl deposit in water vapor at 600°C. Electrochemistry Communications, 12(2): 191-193. https://doi.org/10.1016/j.elecom.2009.11.021

[7] Wu, L., Li, Z., Song, Y. (2009). Field synergy principle of heat and mass transfer. Science Bulletin, 54(24): 4604-4609. https://doi.org/10.1007/s11434-009-0498-3

[8] Vikhnin, V.S., Kapphan, S.E. (2002). New type charge transfer states in ferroelectric oxides: Actual problems. Radiation Effects and Defects in Solids, 157(6-12): 853-856. https://doi.org/10.1080/10420150215821

[9] Qu, X., Song, Y., Liu, D., Cui, X., Peng, Y. (2020). Lithium-ion battery performance degradation evaluation in dynamic operating conditions based on a digital twin model. Microelectronics Reliability, 114: 113857. https://doi.org/10.1016/j.microrel.2020.113857

[10] Terkes, M., Demirci, A., Gokalp, E., Cali, U. (2024). Multi-stage and multi-objective feed-in damping-based battery aging-aware energy management strategy for renewable energy integration. IEEE Access, 12: 161401-161416. https://doi.org/10.1109/access.2024.3468716

[11] Liu, B., Wu, C., Liu, Y., Pan, Y., Li, D., Chu, Z., Zhang, C., Li, H. (2025). Electrochemical-mechanical understanding of the accelerated degradation of lithium-ion batteries caused by mechanical stress. Energy, 333: 137420. https://doi.org/10.1016/j.energy.2025.137420.

[12] Zhang, Z. (2018). Predictions of cyclic yielding behavior of solids based on a nonequilibrium thermodynamic theory. Mechanics of Materials, 118: 85-93. https://doi.org/10.1016/j.mechmat.2017.12.011

[13] Singh, V.P., Cui, H., Byrd, A. (2015). Sediment graphs based on entropy theory. Journal of Hydrologic Engineering, 20(6): C4014004. https://doi.org/10.1061/(asce)he.1943-5584.0001068

[14] Hussain, E.S., Suhael, S.M. (2025). Optimization of HVAC systems: Advances in thermofluid performance modeling and intelligent control strategies. Power Engineering and Engineering Thermophysics, 4(1): 58-85. https://doi.org/10.56578/peet040105

[15] Lebedev, V.A. (2010). Dynamic versions of EMF method in studies of phase formation and thermodynamic properties of metal alloys. Russian Journal of Electrochemistry, 46(6): 646-651. https://doi.org/10.1134/s102319351006008x

[16] Cai, Z., Wu, C., Shen, J., Xu, L., Yu, Q. (2025). The rapid health status estimation of lithium-ion power batteries by short process in the full-voltage domain. Energy Technology, 13(11): 250557. https://doi.org/10.1002/ente.202500557

[17] Feng, X., Weng, C., Ouyang, M., Sun, J. (2016). Online internal short circuit detection for a large format lithium ion battery. Applied Energy, 161: 168-180. https://doi.org/10.1016/j.apenergy.2015.10.019

[18] Messaggi, M., Gambaro, C., Casalegno, A., Zago, M. (2022). Development of innovative flow fields in a vanadium redox flow battery: Design of channel obstructions with the aid of 3D computational fluid dynamic model and experimental validation through locally-resolved polarization curves. Journal of Power Sources, 526: 231155. https://doi.org/10.1016/j.jpowsour.2022.231155

[19] Dong, M., Zhu, B., Tan, F., Liu, G. (2026). IBPS—A novel integrated battery protection system based on novel high-precision pressure sensing. Electronics, 15(5): 1013. https://doi.org/10.3390/electronics15051013

[20] Wu, C., Liang, J., Wang, Y., Li, B. (2025). Online state-of-charge estimation for lithium-ion batteries via a high-degree-of-freedom robust observer with model parameter identification. Energy, 334: 137688. https://doi.org/10.1016/j.energy.2025.137688

[21] Zhang, J., Chen, J., Liu, D., He, L., Yang, K., Du, F., Ye, W., Zhang, X. (2025). Multi-state joint prediction algorithm for lithium battery packs based on data-driven and physical models. Energy, 322: 135641. https://doi.org/10.1016/j.energy.2025.135641